An Unstructured Finite-Volume Method for Structure-Electrostatics Interactions in MEMS

Shankhadeep Das [a] , Sanjay R. Mathur [a] & Jayathi Y. Murthy [a]

[a] NNSA PRISM: Center for Prediction of Reliability, Integrity and Survivability of Microsystems and School of Mechanical Engineering, Purdue University, West Lafayette, Indiana, USA

Available online: 02 Dec 2011

PLEASE SCROLL DOWN FOR ARTICLE

AN UNSTRUCTURED FINITE-VOLUME METHOD FOR STRUCTURE–ELECTROSTATICS INTERACTIONS IN MEMS

Shankhadeep Das, Sanjay R. Mathur, and Jayathi Y. Murthy

NNSA PRISM: Center for Prediction of Reliability, Integrity and Survivability of Microsystems and School of Mechanical Engineering, Purdue University, West Lafayette, Indiana, USA

Radio-frequency microelectromechanical systems (RF MEMS) are widely used for contact actuators and capacitive switches, and involve metal–dielectric contact. In these devices, the structure is activated by an electrostatic force, whose magnitude changes as the gap closes. It is advantageous to model fluid and structural mechanics and electrostatics within a single comprehensive numerical framework to facilitate coupling between them. In this article, we extend a cell-based finite-volume approach popularly used to simulate fluid flow to characterize structure–electrostatics interactions. The method employs fully implicit second-order finite-volume discretization of the integral conservation equations governing elastic solid mechanics and electrostatics, and uses arbitrary convex polyhedral meshes. Results are presented in this article for a fixed-fixed beam under electrostatic actuation.

1. INTRODUCTION

Radio-frequency microelectromechanical systems (RF MEMS) have wide applicability in contact actuators and capacitive switches, and involve a fixed-fixed metallic membrane which makes repeated mechanical contact with a thin dielectric film [1, 2], as shown in Figure 1. In these devices, the membrane deforms under electrostatic actuation, the magnitude of which increases nonlinearly as the gap width decreases. Although these devices hold great promise for both civilian and defense applications, they are prone to failure. Accurate modeling and simulation of these devices is necessary to better understand failure mechanisms, and to improve their performance. Since this is a fully coupled multiphysics problem, it is advantageous to develop a single comprehensive numerical framework for fluid and structural analysis and electrostatics.

Over the years, finite-element (FE) methods have traditionally been used for solid-body stress analysis, whereas finite-volume (FV) methods have been used for

NOMENCLATURE

$\mathbf{A}$	outward-pointing area vector		δ_{xx}	percentage absolute error in σ_{xx}
A_{eff}	effective electrode area		Δt	time step
Co	Courant number		Δx	cell dimension
$\mathbf{D}$	diffusion flux vector at cell face		ε	deformation strain tensor
E	Young's modulus		ε_{air}	permittivity of air
$\widehat{E}$	modified Young's modulus		ε_0	permittivity of free space
$\mathbf{F}$	force on face f		λ	Lamé's coefficient
F_{elec}	electrostatic force		μ	Lamé's coefficient
F_m	restoring mechanical force on the beam		ν	Poisson's ratio
			ρ	density
$\mathbf{G}$	gradient of the displacement vector		σ	stress tensor
I	second moment of inertia		σ_t	surface charge density
$\mathbf{I}$	unit tensor		τ	shear stress
L	length of beam		ϕ	electrostatic potential
M	flux Jacobian		$\mathbf{\Psi}$	secondary gradient component of diffusion flux
$\mathbf{R}$	residual vector			
V	cell volume			

V_{PI}	pull-in voltage
b	width of beam
$\mathbf{b}$	source vector
ds	distance between centroids of cells C_0 and C_1
$\mathbf{e}_\xi$	unit vector connecting cell centroids
$\mathbf{f}$	body force vector per unit volume
g	gap width
g_0	gap width with zero applied voltage
h	thickness of beam
n	surface normal
$\mathbf{r}$	position vector
t	time
$\mathbf{t}$	traction vector
u	wave speed
$\mathbf{w}$	displacement vector
$\mathbf{x}$	solution vector
Ω	natural frequency of beam
α	uniform load per unit length
δ_{ij}	Kronecker delta

Subscripts

$()_b$	value of the argument on boundary b
$()_n$	component normal to the boundary surface
$()_t$	component tangential to the boundary surface
$()_i$	component in the i direction
$()_x$	component in the x direction
$()_y$	component in the y direction
$()_f$	associated with cell face f
$()_0$	associated with cell C_0
$()_1$	associated with cell C_1
$()_{\text{nb}}$	associated with neighboring cell C_{nb}

Superscripts

$()^N$	value of the argument at current time level N
$()^T$	transpose of the argument tensor
$()^*$	nondimensional value of the argument

modeling fluid flow and heat transfer problems. A popular FE approach is to solve the governing differential equations by the method of weighted residuals, and employ predefined shape functions to approximate the variation of the physical variables across element boundaries [3]. FV methods, on the other hand, usually employ second-order spatial discretization of the integral form of the conservation equations as the starting point [4]. The main advantage of the FV methods is that they ensure conservation of transported variables. They can easily incorporate coupling and non-linearity, and are most commonly solved sequentially using iterative solvers. This is also advantageous in terms of memory requirement for large computational meshes.

Although there are significant differences in the FE and FV approaches, they essentially solve for similar forms of the governing equations. In fact, FV methods
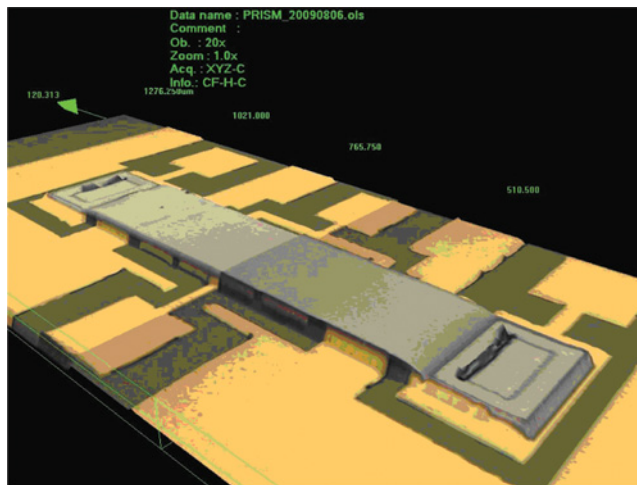
Figure 1. RF MEMS device showing nickel membrane, contact pads, and anchors [2] (color figure available online).

may be considered to be a particular instance of the method of weighted residuals, with non-Galerkin weighting [5]. It has been shown that the two schemes are equivalent in many respects [6]. This has motivated the researchers to apply FV schemes for structural analyses and FE schemes for fluid flows. Over the last two decades, various researchers have tried to model multiphysics problems within either the FE or FV framework. On the FE side, the use of finite-element techniques for modeling fluid flows has been described by various researchers [7–9]. Finite-element models have also been developed to study fluid–structure interaction (FSI) problems [10–12]. The deforming-spatial-domain/stabilized space-time (DSD/SST) methodology has been extensively used to simulate fluid flows with moving boundaries [13–16]. The flow-condition-based interpolation (FCBI) scheme proposed by Bathe [17–20] to model incompressible flows has been applied to study general fluid flows with structural interactions [21, 22]. Within the FV framework, Demirdžić et al. [23] first developed a cell-based FV approach to study thermoelastic problems. This method has subsequently been extended to unstructured meshes in complex geometries [24], and to study coupled heat transfer, fluid flow, and stress analysis problems [25]. The cell-based FV scheme has also been applied to study linear elastic problems [26], thermo-elasto-plastic stress analysis [27], and thermo-elastic problems in anisotropic materials [28]. Research has also been carried out to develop a vertex-based FV scheme to study elastic solid mechanics problems on unstructured meshes [29, 30]. This scheme has also been extended to study elastic/visco-plastic problems [31], dynamic structural response of elastic solid domains [32], and dynamic fluid–structure interaction problems [33]. A major advantage of the cell-centered approach is that force balance on a control volume can be done very easily as a flux balance on the control-volume faces.

In the 1970s, finite-volume-based approaches were developed to study fluid flows on simple geometries [34, 35]. These techniques were subsequently extended

to unstructured meshes [25, 36]. The desire to extend finite-volume methods to irregular complex geometries also led to the development of control-volume finite-element methods (CVFEM) which combined features of finite-element and finite-volume methods [37, 38]. These methods ensured conservation of transported variables, while maintaining the geometric flexibility associated with finite-element methods. Over the last three decades, a number of formulations of both finite-volume and control-volume finite-element methods have been developed for a wide variety of applications including single-phase fluid flows [39, 40], multiphase flows [41, 42], solid–liquid phase change [43], conduction, convection, and radiative heat transfer [44–46], submicron thermal transport [47], solid-body stress analysis [23–33], and combustion [48]. However, the potential of these techniques in developing a unified formulation for studying multiphysics problems in RF MEMS was never recognized.

    In this article we extend the cell-centered FV formulation to study the multiphysics problem of structural deformation of fixed-fixed beams under electrostatic actuation. In comparison to similar approaches tried in the past [24–26], the present method employs complete linearization of the stress tensor, which improves the convergence rate by over two orders of magnitude and is also beneficial in terms of stability for transient problems. Details of the discretization scheme are presented in this article. The solver is applied to a variety of steady-state and transient problems, and is shown to perform satisfactorily by comparison to the analytical solution on these test cases. It is next applied to study structure–electrostatics interaction in MEMS. A variable electrostatic force is assumed for this problem, and differences with the case of constant electrostatic force are shown. Finally, quasi-static and dynamic pull-in voltages of an RF MEMS device are computed.

2. GOVERNING EQUATIONS

    The governing equation for elastic solid-body equilibrium is

$$\frac{\partial^2(\rho \mathbf{w})}{\partial t^2} - \nabla \cdot \sigma = \rho \mathbf{f} \tag{1}$$

where $\mathbf{w}$ is the displacement vector, ρ is the density, $\mathbf{f}$ is the body force vector per unit volume, and σ is the stress tensor. The strain tensor ε is defined as

$$\varepsilon = \frac{1}{2} [\nabla \mathbf{w} + (\nabla \mathbf{w})^T] \tag{2}$$

For the case of an elastic solid body, the stress tensor is related to the strain tensor ε by Hooke's law:

$$\sigma = 2\mu\varepsilon + \lambda \operatorname{tr}(\varepsilon)\mathbf{I} \tag{3}$$

In the above equation, $\mathbf{I}$ is the unit tensor, μ and λ are the Lamé coefficients, and are given by

$$\mu = \frac{E}{2(1 + \nu)} \tag{4}$$

$$\lambda = \begin{cases} \frac{\nu E}{(1+\nu)(1-\nu)} & \text{for plane stress} \\[2mm] \frac{\nu E}{(1+\nu)(1-2\nu)} & \text{for plane strain} \end{cases} \tag{5}$$

where ν is Poisson's ratio and E is Young's modulus. Using Eqs. (2), (3), (4), and (5), Eq. (1) can be written as

$$\frac{\partial^2(\rho\mathbf{w})}{\partial t^2} - \nabla \cdot [\mu\nabla\mathbf{w} + \mu(\nabla\mathbf{w})^T + \lambda\mathbf{I}\,\text{tr}(\nabla\mathbf{w})] = \rho\mathbf{f} \tag{6}$$

3. FINITE-VOLUME DISCRETIZATION

The governing equation is discretized using the finite-volume discretization scheme. The computational domain is divided into arbitrary convex polyhedral meshes. The displacement vector is stored at the cell centroids. The governing equation for structural dynamics is integrated over the control volumes C_0, shown in Figure 2, to yield cell balances of inertial, surface, and body force terms as follows:

$$\int_{V_o} \frac{\partial^2(\rho\mathbf{w})}{\partial t^2}\, \mathrm{d}V - \oint_{\partial V_o} d\mathbf{A} \cdot [\mu\nabla\mathbf{w}] = \oint_{\partial V_o} d\mathbf{A} \cdot [\mu(\nabla\mathbf{w})^{\mathrm{T}} + \lambda\,\mathbf{I}\,\text{tr}(\nabla\mathbf{w})] + \int_{V_o} \rho\mathbf{f}\, dV \tag{7}$$

3.1. Rate of Change

Equation (7) is discretized using a partially implicit discretization scheme. The temporal derivative is calculated using a first-order backward differencing procedure, using three consecutive time levels as follows:

$$\int_{V_o} \frac{\partial^2(\rho\mathbf{w})}{\partial t^2} dV = \frac{(\rho V)_o}{(\Delta t)^2}(\mathbf{w}^N - 2\mathbf{w}^{N1} + \mathbf{w}^{N2})_o \tag{8}$$

where $\mathbf{w}^N$ is the displacement vector at the current time level, $\mathbf{w}^{N1}$ and $\mathbf{w}^{N2}$ are the displacement vectors at the previous two time levels, and the time increment is given by $\Delta t = t^N - t^{N1}$.
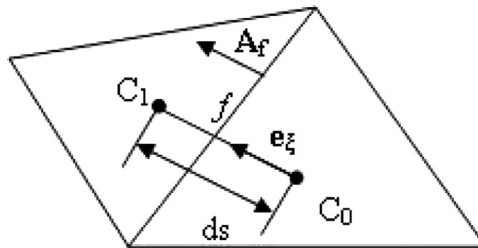

Figure 2. Nomenclature associated with cells C_0 and C_1 for calculation of diffusion flux in unstructured meshes.

3.2. Diffusion Term

The second term on the left-hand side (LHS) of Eq. (7) has the form of a standard diffusion term in a typical finite-volume method (FVM) and is treated implicitly as

$$\mathbf{D}_f = \oint_{\partial V_o} d\mathbf{A} \cdot [\mu \nabla \mathbf{w}] = \sum_f \mu_f \mathbf{A}_f \cdot (\nabla \mathbf{w})_f \tag{9}$$

where μ_f, $\mathbf{A}_f$, and $(\nabla \mathbf{w})_f$ are the Lamé coefficient, the outward-pointing area vector, and the gradient of the displacement vector associated with the face f, respectively. For unstructured meshes, the diffusion term can be decomposed into the primary gradient and secondary gradient components [49], and written in the following way:

$$\mathbf{D}_f = \frac{\mu_f}{ds} \frac{\mathbf{A}_f \cdot \mathbf{A}_f}{\mathbf{A}_f \cdot \mathbf{e}_\xi} (\mathbf{w}_1 - \mathbf{w}_0) + \Psi_f \tag{10}$$

Here $\mathbf{e}_\xi$ is the unit vector aligned with the line joining the centroids of the two cells C_0 and C_1 on either side of the face f, as shown in Figure 2, and $\mathbf{w}_0$ and $\mathbf{w}_1$ are the displacement vectors in cells C_0 and C_1. The quantity Ψ_f is the secondary gradient term, and is nonzero only for nonorthogonal meshes.

3.3. Transpose and Divergence Terms

Two different formulations of the transpose and divergence parts of the stress tensor are considered. In the first case, the transpose and divergence terms are included in an explicit source term. In the second case, these terms are linearized completely. We describe each approach in turn.

Formulation 1: Explicit Source Term. In this treatment, the transpose and divergence parts of the stress tensor are treated in an explicit manner, and therefore included in the source term, along with the body force term:

$$\oint_{\partial V_o} d\mathbf{A} \cdot [\mu(\nabla \mathbf{w})^T + \lambda \mathbf{I} \operatorname{tr}(\nabla \mathbf{w})] + \int_{V_o} \rho \mathbf{f} \, dV = \sum_f \mu_f \mathbf{A}_f \cdot (\nabla \mathbf{w})_f^T$$
$$+ \sum_f \lambda_f \mathbf{A}_f \cdot \mathbf{I} \operatorname{tr}(\nabla \mathbf{w})_f + (\rho \mathbf{f} V)_0 \tag{11}$$

Here the subscript f denotes the face value. The face value of $\nabla \mathbf{w}$ in Eq. (11) is found as the linear interpolant of the gradients in the cells C_0 and C_1. In this approach, the primary diffusion term [the first term on the RHS of Eq. (10)] is treated implicitly, but the secondary gradient term Ψ_f and all the terms in Eq. (11) are treated explicitly. The resulting scheme has implicit coupling only to face-neighbor displacements in the same coordinate direction, but not to displacements in other coordinate directions. The computational stencil thus consists only of face-neighbor cells of C_0. This approach has previously been taken by Demirdžić and Muzaferija [24, 25].

Formulation 2: Complete Linearization of Stress Tensor. The explicit treatment described above has poor convergence rate and requires extensive under-relaxation to obtain convergence of iterative procedures. This is because the explicit part of the stress tensor ensures coupling between different directions, and hence carries more information than the implicit part [26]. This motivates us to implement complete linearization of the stress tensor. We first calculate the cell gradient using the linear least-squares approach [50] in the following way:

$$\nabla\phi_0 = \sum_{nb} g_{nb}(\phi_{nb} - \phi_0) \tag{12}$$

where ϕ_0 can be any scalar or vector in the cell C_0, ϕ_{nb} is the value of the corresponding scalar or vector in the neighboring cell C_{nb}, and $\mathbf{g}_{nb}$ is a function of the mesh geometry. We then define G_{ij} as

$$G_{ij} = \frac{\partial w_i}{\partial x_j} \tag{13}$$

where w_i is the ith component of displacement vector. The derivative of G_{ij} with respect to the kth component of the displacement vector is given as

$$\frac{\partial}{\partial w_{0,k}}\left(G_{0,ij}\right) = -\sum_{nb} g_{nb,j}\delta_{ik}$$

$$\frac{\partial}{\partial w_{nb,k}}\left(G_{0,ij}\right) = g_{nb,j}\delta_{ik} \tag{14}$$

Here $G_{0,ij}$ denotes the value of G_{ij} in the cell C_0, $w_{0,k}$ and $w_{nb,k}$ denote the kth component of the displacement vector in the cells C_0 and C_{nb}, respectively, and δ_{ik} is the Kronecker delta. The force on any face f is given by

$$\mathbf{F} = \mu\mathbf{A}_f \cdot (\nabla\mathbf{w})_f + \mu\mathbf{A}_f \cdot (\nabla\mathbf{w})_f^T + \lambda\mathbf{A}_f \cdot \mathbf{I}\,\mathrm{tr}(\nabla\mathbf{w})_f \tag{15}$$

Again, the subscript f denotes the face value. We denote the individual components of $\mathbf{F}$ as $\mathbf{F}_1$, $\mathbf{F}_2$, and $\mathbf{F}_3$, where $\mathbf{F}_1$, $\mathbf{F}_2$, and $\mathbf{F}_3$ are given by

$$\mathbf{F}_1 = \mu\mathbf{A}_f \cdot (\nabla\mathbf{w})_f$$

$$\mathbf{F}_2 = \mu\mathbf{A}_f \cdot (\nabla\mathbf{w})_f^T$$

$$\mathbf{F}_3 = \lambda\mathbf{A}_f \cdot \mathbf{I}\,\mathrm{tr}(\nabla\mathbf{w})_f \tag{16}$$

It may be shown that

$$\frac{\partial F_{1i}}{\partial G_{kl}} = \mu A_l\delta_{ik}$$

$$\frac{\partial F_{2i}}{\partial G_{kl}} = \mu A_k\delta_{il}$$

$$\frac{\partial F_{3i}}{\partial G_{kl}} = \lambda A_i\delta_{kl} \tag{17}$$

The required components of the Jacobian are $\partial F_i / \partial w_j$, which may be computed using the chain rule as

$$\frac{\partial F_i}{\partial w_j} = \sum_k \sum_l \left(\frac{\partial F_{1i}}{\partial G_{kl}} + \frac{\partial F_{2i}}{\partial G_{kl}} + \frac{\partial F_{3i}}{\partial G_{kl}} \right) \frac{\partial G_{kl}}{\partial w_j} \tag{18}$$

Since the face gradient $\nabla \mathbf{w}$ is an average of the gradients in cells C_0 and C_1, the derivative $\partial F_i / \partial w_j$ is nonzero with respect to the displacements w_k in cells C_0, C_1, and all their face-neighbor cells. The Jacobian entries $\partial F_{2i} / \partial w_j$ and $\partial F_{3i} / \partial w_j$ lead to implicit coupling between the displacements in different coordinate directions. Furthermore, their inclusion expands the normal stencil of cells included in typical cell-centered finite-volume discretizations such as those used in [24, 25].

The Jacobian of the residual for cell C_0 is

$$\frac{\partial \mathbf{R}}{\partial \mathbf{w}} = \sum_f \frac{\partial \mathbf{F}}{\partial \mathbf{w}} + \left(\frac{\partial \mathbf{S}}{\partial \mathbf{w}} \right) \tag{19}$$

where $\mathbf{R}$ is the residual of the discrete equation and the summation is over all the faces of the cell. The first term in Eq. (19) is the contribution to the Jacobian of the forces on the faces of the cell C_0, while the second term is the contribution of source and unsteady terms. Newton linearization of the equation $\mathbf{R} = \mathbf{0}$ employs the Jacobian in Eq. (19). This procedure enables the complete linearization of the governing structural deformation equation. This allows the fully implicit treatment of the stress tensor and dramatically improves the convergence rate.

To our knowledge, this is the first published attempt to linearize the entire stress tensor in a cell-based finite-volume scheme. Nearly all published FVM-based stress analysis techniques employ Formulation 1 [24, 25]. Jasak and Weller [26] sought to improve the convergence of their cell-based scheme through partial linearization, including parts of the transpose and divergence terms in the diffusion term, but leaving the rest of the stress tensor explicit. In our experience, this approach alleviates convergence problems somewhat, but does not entirely cure them.

4. STRUCTURE–ELECTROSTATICS INTERACTION IN MEMS

A schematic of the MEMS device is shown in Figure 3. The electrostatic field in the air gap is governed by the following equation:

$$\nabla^2 \phi = 0 \quad \text{in air} \tag{20}$$

Here ϕ represents the electrostatic potential. The surface charge density σ_t on the top electrode can be represented as

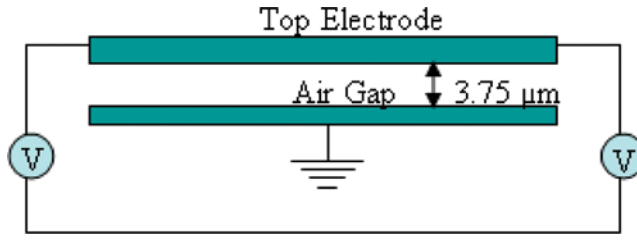$$\sigma_t = -\varepsilon_{\text{air}} \left[\frac{\partial \phi}{\partial n} \right]_{\text{air}} \tag{21}$$

Figure 3. Simplified representation of an RF MEMS (color figure available online).

where ε_{air} is the permittivity of air, and n represents the normal to the surface. An analytical expression for the electrostatic force F_{elec} on the top electrode can be obtained as [51]

$$F_{elec} = b \int_0^L \left[\frac{\sigma_t^2(x)}{2\varepsilon_{air}} \right] dx \qquad (22)$$

where b and L represent the width and length of the electrode. The top electrode is assumed to be an equipotential surface. The deforming membrane and the domain outside it are separately meshed, with the two meshes being conformal at the interface, as shown in Figure 4a.
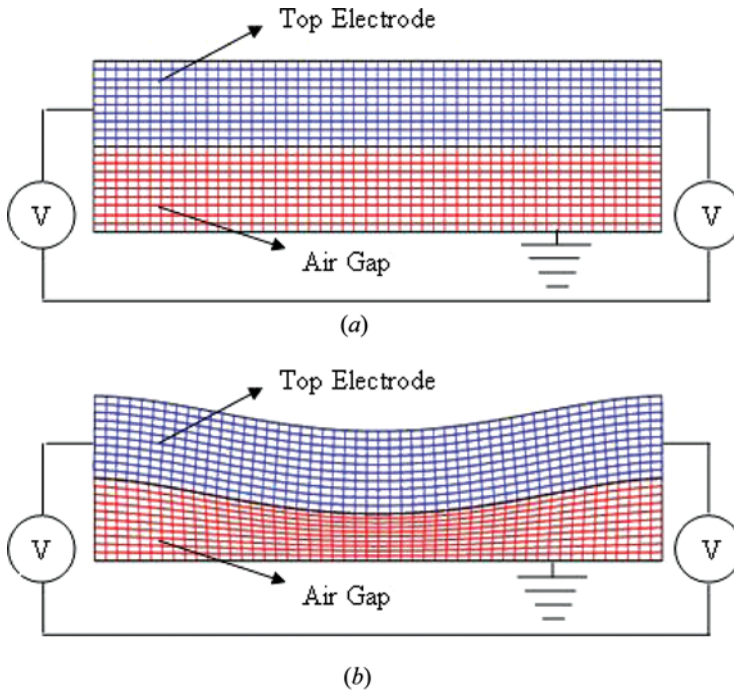

Figure 4. RF MEMS: (a) undeformed state; (b) deformed state (color figure available online).

The FVM discretization of the potential equation involves the integration of Eq. (20) over the control volumes C_0, and the application of the divergence theorem to yield

$$\oint_{\partial V_o} d\mathbf{A} \cdot [\nabla \phi] = \sum_f \mathbf{A}_f \cdot (\nabla \phi)_f = 0 \qquad (23)$$

Here $(\nabla \phi)_f$ represents the gradient of the electrostatic potential associated with face f. For unstructured meshes, Eq. (23) can be decomposed into the primary gradient and secondary gradient components [49], and written in the following way:

$$\frac{1}{ds} \frac{\mathbf{A}_f \cdot \mathbf{A}_f}{\mathbf{A}_f \cdot \mathbf{e}_\xi} (\phi_1 - \phi_0) + \kappa_f = 0 \qquad (24)$$

where κ_f is the secondary gradient term associated with face f, and is nonzero for nonorthogonal meshes only. As explained in [49], the first term in Eq. (24) is treated implicitly, while the second is treated explicitly in the equation system.

5. INITIAL AND BOUNDARY CONDITIONS

5.1. Structure Model

For transient problems, $\mathbf{w}$ and $\partial \mathbf{w}/\partial t$ must be specified at time $t = 0$. The boundary condition can be of the following types:

1. Specified displacement
2. Specified traction
3. Symmetry
4. Free surface (zero traction)

For the specified displacement boundary condition (Dirichlet boundary condition) we have

$$\mathbf{w}(\mathbf{r}) = \mathbf{w}_b \qquad \mathbf{r} \in \mathbf{A} \qquad (25)$$

where $\mathbf{r}$ is the position vector on the surface $\mathbf{A}$, and $\mathbf{w}_b$ is the specified displacement vector on the surface of the boundary. For specified traction or free-surface (zero-traction) boundary conditions (Neumann boundary conditions) we have

$$\mathbf{t}(\mathbf{r}) = \mathbf{t}_b \qquad \mathbf{r} \in \mathbf{A} \qquad (26)$$

Here $\mathbf{t}_b$ is the specified traction on the boundary. For symmetry boundary conditions we have

$$w_n = 0 \qquad \frac{\partial w_t}{\partial n} = 0 \qquad (27)$$

where n is the normal to the symmetry boundary surface, and w_n and w_t are the displacement components normal and tangential to the symmetry surface.

5.2. Electrostatics Model

For the electrostatics model, only two types of boundary conditions are used:

1. Specified potential
2. Specified potential gradient

For the specified potential boundary condition (Dirichlet boundary condition) we have

$$\phi(\mathbf{r}) = \phi_b \qquad \mathbf{r} \in \mathbf{A} \tag{28}$$

where $\mathbf{r}$ is the position vector on the surface $\mathbf{A}$, and ϕ_b is the specified potential on the surface of the boundary. For specified potential gradient boundary condition (Neumann boundary condition) we have

$$\frac{d\phi}{d\mathbf{r}}(\mathbf{r}) = \phi'_{\mathbf{b}} \qquad \mathbf{r} \in \mathbf{A} \tag{29}$$

Here ϕ'_b is the specified potential gradient on the boundary.

6. MESH MOTION STRATEGY

The application of electrostatic force on the membrane causes the membrane to deform, and distorts the domain on which the potential equation is solved, as shown in Figure 4b. Hence a strategy for mesh deformation must be implemented. Mesh deformation is handled following the procedure developed in [52]. To explain the mesh deformation procedure, a sample 2-D mesh is shown in Figure 5. The domain has fixed walls on the left and right sides, whereas the displacement is specified on the top and bottom surfaces. First, for every internal node (i_s), the node on the moving wall (i_{swall}) that is closest to it is determined by an efficient KD-tree-based search algorithm [53]. The distance between i_s and i_{swall} is identified as $d(i_s)$. The maximum of all $d(i_s)$ is denoted by d_{max}. Then the deformation $\boldsymbol{\delta r}(i_s)$ of the internal node i_s is
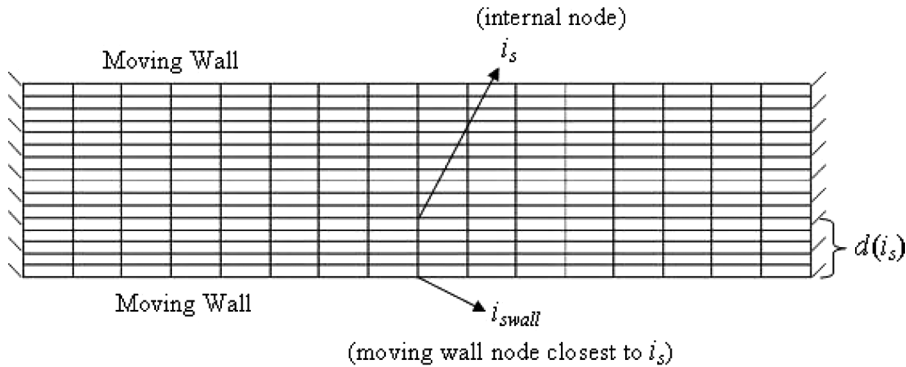

Figure 5. Nomenclature for mesh deformation.

obtained as the product of a distance function $f(i_s)$ and the specified deformation $\delta\mathbf{r}(i_{swall})$ of the closest wall node i_{swall} as follows:

$$\delta\mathbf{r}(i_s) = f(i_s)\delta\mathbf{r}(i_{swall}) \tag{30}$$

The function $f(i_s)$ is obtained using two exponential damping functions:

$$f(i_s) = \frac{f_2^2(i_s)}{f_1^2(i_s) + f_2^2(i_s)} \tag{31}$$

Here $f_1(i_s)$ and $f_2(i_s)$ are given by the following relations:

$$f_1(i_s) = \frac{1 - \exp[-d(i_s)/d_{max}]}{(e-1)/e} \tag{32}$$

$$f_2(i_s) = \frac{1 - \exp[1 - d(i_s)/d_{max}]}{(1-e)} \tag{33}$$

The function $f(i_s)$ has a value close to 1 for internal nodes close to the moving walls, and tends to 0 when $d(i_s)$ approaches d_{max}. This produces a rigid grid near the walls and far away from the walls. However, rest of the areas is elastic and can be easily deformed. In large-deformation problems, the above procedure may not be sufficient to produce a valid mesh. Thus the calculated deformation of every internal node is further smoothed out using a spring analogy. The deformation $\delta\mathbf{r}_k$ of node k is determined as the weighted average of the deformations of the neighboring nodes:

$$\delta\mathbf{r}_k = \frac{\sum_{i=1}^{nnodes(k)} k_i \delta r_i}{\sum_{i=1}^{nnodes(k)} k_i} \tag{34}$$

Here nnodes (k) is number of nodes surrounding node k, and the weight k_i is equal to the inverse of the distance between the node k and the neighboring node i. This procedure ensures that if the mesh is dense in some sensitive regions of the domain, then even after mesh deformation the mesh will remain dense in those regions.

7. SOLUTION METHODOLOGY

The flowchart for the solution methodology is shown in Figure 6. A sequential solution procedure is used to couple structure and electrostatics. At the beginning of each time step, the forces on the structure domain are computed, following which one iteration of the structural solver is performed. The cell-centered structure displacements thus obtained are interpolated to obtain nodal displacements, which are then used to deform the structure. The nodal displacement for the structure mesh at the structure–electrostatics interface is used as a specified displacement boundary condition for deformation of the mesh on which the electrostatics model is solved. The electrostatics mesh is then deformed using the previously described mesh
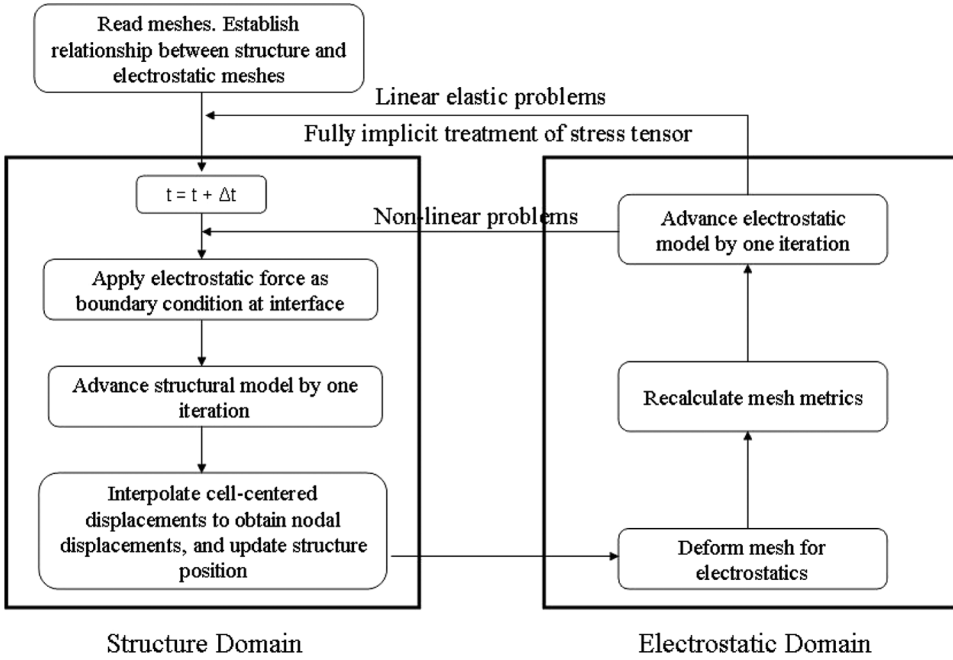
Figure 6. Flowchart showing solution methodology.

deformation procedure, and the mesh metrics are recalculated. The electrostatics model is then solved on the electrostatics mesh. The above procedures within each time step constitute an outer iteration loop. If Formulation 2 is used for discretizing the stress tensor for the structure, only one outer iteration need be performed within each time step for linear elastic problems. However, for nonlinear problems, multiple outer iterations are performed before time is advanced to the next time step.

For either domain (structure or electrostatics), the discretization procedure described above gives rise to a set of linear algebraic equations of the form

$$M\mathbf{x} + \mathbf{b} = 0 \tag{35}$$

where M is a symmetric and diagonally dominant $N \times N$ sparse matrix, $\mathbf{x}$ is a vector containing the values of the displacement vector components at the N control volumes, and $\mathbf{b}$ is the source vector. The system of algebraic equations can be solved iteratively with a BCGSTAB solver [54]. Equation (35) can also be represented as

$$M\delta + \mathbf{R} = 0 \tag{36}$$

where $\mathbf{R}$ is the residual, and δ is given as

$$\delta = \mathbf{x}^{k+1} - \mathbf{x}^k \tag{37}$$

Here $\mathbf{x}^k$ is the solution at the kth iteration.

For the structural solution, if explicit source treatment is being used, it is not necessary to solve the above system of equations to a tight tolerance, since the source vector **b** contains explicit terms. Therefore reduction of residuals by an order of magnitude is considered sufficient. In this case, once the above system of equations is solved, the source vector **b** is updated using the newly available values of the displacement vector and the process is repeated [24]. Thus it is necessary to have an outer iteration loop, and the procedure is considered converged when the sum of the normalized absolute residuals has decreased by 3–4 orders of magnitude for each displacement component. For transient problems, this procedure is repeated for each time step.

On the other hand, if the stress tensor is linearized completely, for linear elastic problems, the system of discretized algebraic equations for the structure can be solved within one outer iteration if the convergence criterion for inner iterations in the linear solver is set to a low enough value. For transient problems, this procedure is repeated for each time step.

8. RESULTS

In this section, we first present a number of tests of algorithm performance, and then apply the proposed method to the solution of structure–electrostatics interaction in MEMS.

8.1. Comparison of Explicit and Implicit Stress Linearization

To test the efficacy of this linearization scheme, we study the problem of steady-state deformation of a fixed-fixed beam due to uniform loading. A schematic of the beam is shown in Figure 7. The solution to the problem is given by the Euler-Bernoulli beam theory, and the deflection of the beam is given as

$$w_y = \frac{\alpha x^2 (L - x)^2}{24EI} \tag{38}$$

where α is the force per unit length, E is Young's modulus, I is the second moment of inertia, and L is the length of the beam. A 16×160 mesh is selected for this simulation based on a mesh convergence study, and a plane stress condition is assumed.
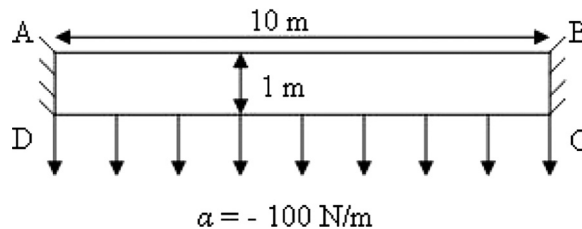

Figure 7. Fixed-fixed beam subjected to uniform loading.

Young's modulus of the material is $E = 200\,\mathrm{GPa}$, and Poisson's ratio is $\nu = 0.31$. The problem is solved by two methods. Formulation 1 denotes the case which involves splitting up of the stress tensor into implicit and explicit parts, and Formulation 2 denotes the case of complete linearization of the stress tensor. For Formulation 1, the reduction of residuals by an order of magnitude is taken as the convergence criterion for the inner iteration loop in the linear solver, while the reduction of the global residuals by 8 orders of magnitude is taken as the convergence criterion for the outer iteration loop. For Formulation 2, the reduction of the residuals by 9 orders of magnitude is set as the convergence criterion for both the inner and outer iteration loops. Formulation 1 took 998 outer iterations and 113.67 s, whereas Formulation 2 took only 1 outer iteration and 0.57 s for completion. This shows that the complete linearization scheme in Formulation 2 has decreased the computational time by approximately a factor of 200. Therefore this scheme will henceforth be used to discretize the governing equations for all structural problems described in this article.

8.2. Static Deformation of Fixed-Free Cantilever Beam

The first verification test of the FVM solver consists of a cantilever beam, shown in Figure 8, with concentrated load at the free end [29]. To simulate this problem, a zero-displacement boundary condition is specified on the surface AD, whereas traction-free boundary conditions are specified on the surfaces AB, BC, and CD. A downward vertical surface force is specified on the face of the control volume adjacent to the node C, and directly added to the force balance for that control volume. A plane stress condition is used for this problem. Young's modulus of the material is $E = 210\,\mathrm{GPa}$, and Poisson's ratio is $\nu = 0.25$. The horizontal and vertical displacements of node C can be derived analytically as $w_x = -0.3125\,\mu\mathrm{m}$ and $w_y = -2.16\,\mu\mathrm{m}$. A mesh convergence study is performed on this problem. Table 1 shows the percent errors in the x displacement of node C for different mesh sizes. The errors are computed with respect to the analytical horizontal displacement for node C. Results show that the error decreases to 0.25% for the 32×320 mesh. The FVM displacements of node C obtained with this mesh are $w_x = -0.3117\,\mu\mathrm{m}$ and $w_y = -2.153\,\mu\mathrm{m}$. The results show that the FVM scheme accurately calculates the displacements for node C.
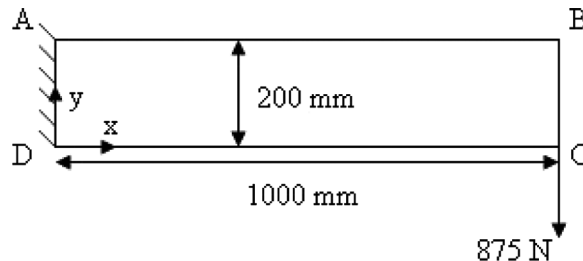

Figure 8. Cantilever beam with concentrated load at the free end.

Table 1. Mesh convergence study for static deformation of cantilever beam

Mesh size	Percent error in x displacement
4×40	23.39
8×80	11.61
16×160	4.59
32×320	0.25

8.3. Stress Concentration around Circular Hole

The model problem [24, 26, 55] consists of a plate with a circular hole which is subjected to unidirectional tensile load, as shown in Figure 9. For infinitely large plates in which the hole radius is small compared to the plate dimensions, the analytical stress distribution is given by [56]

$$\sigma_{xx} = t_x \left[1 - \frac{a^2}{r^2} \left(\frac{3}{2} \cos 2\theta + \cos 4\theta \right) + \frac{3}{2} \frac{a^4}{r^4} \cos 4\theta \right]$$

$$\sigma_{yy} = t_x \left[-\frac{a^2}{r^2} \left(\frac{1}{2} \cos 2\theta - \cos 4\theta \right) - \frac{3}{2} \frac{a^4}{r^4} \cos 4\theta \right] \tag{39}$$

$$\sigma_{xy} = t_x \left[-\frac{a^2}{r^2} \left(\frac{1}{2} \sin 2\theta + \sin 4\theta \right) + \frac{3}{2} \frac{a^4}{r^4} \sin 4\theta \right]$$

where a is the radius of the hole, t_x is the applied tensile load, and $r = \sqrt{x^2 + y^2}$ and $\theta = \tan^{-1} y/x$ represent the polar coordinates. Due to the symmetry of the problem, only one-fourth of the domain is simulated, as shown in Figure 9. Tractions calculated from the analytical solution are imposed as boundary conditions on faces BC and CD, whereas symmetry boundary conditions are imposed on faces AB and DE. The circular arc AE is assumed to be a free surface (zero traction). We use nonorthogonal meshes for this problem. A sample mesh for this problem is shown in Figure 10. A plane strain condition is assumed. Young's modulus of the material is $E = 10^7$ Pa, and Poisson's ratio is $\nu = 0.3$. The applied tensile load is $t_x = 10^4$ Pa.
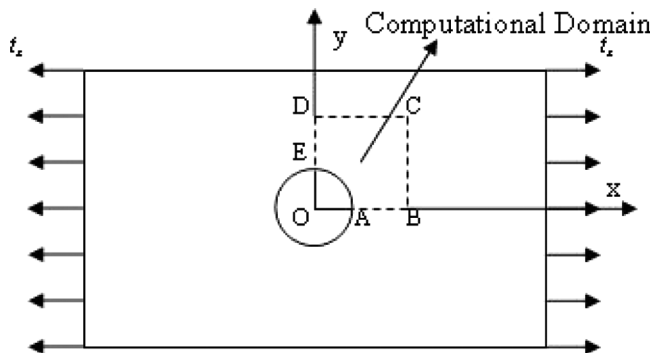

Figure 9. Plate with a circular hole at the center loaded by uniform unidirectional tensile stress (OA $= 0.5$ m, AB $=$ ED $= 1.5$ m, BC $=$ CD $= 2$ m).
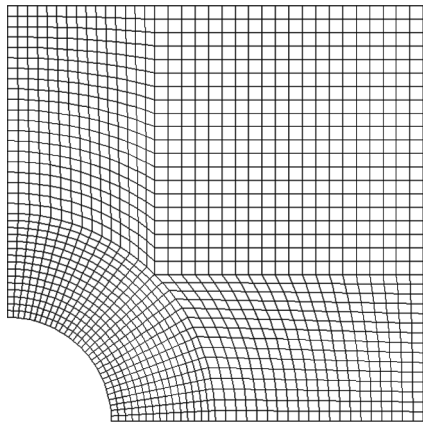
Figure 10. Computational mesh for stress concentration problem.

A mesh convergence study is first performed. For this purpose, the volume-weighted root-mean-square (RMS) errors in the stresses are computed for different mesh sizes. The RMS error is defined as

$$\text{RMS}_{\sigma_{xx}} = \sqrt{\frac{\sum_{i=1}^{N} V_i (\sigma_{xx,\text{analytical}} - \sigma_{xx,\text{fvm}})^2}{\sum_{i=1}^{N} V_i}} \tag{40}$$

Here V_i denotes the volume of cell i. The volume-weighted RMS errors in σ_{xx} are presented in Table 2. It is observed that the RMS error is less than 0.2%, with respect to the applied tensile load of $t_x = 10^4$ Pa, for even the coarsest mesh with 1,450 cells, and decreases to 0.006%, for the mesh with 98,000 cells. Therefore, this mesh is used for plotting the contours of the stress distribution. The contours of σ_{xx}, σ_{yy}, and σ_{xy} are shown in Figure 11 for the FV scheme. The contours of the percentage absolute errors in the stresses, with respect to the applied tensile load, are plotted in Figure 12 for the mesh with 1,450 cells. The errors are defined as

$$\delta_{xx} = \frac{\text{abs}(\sigma_{xx,\text{analytical}} - \sigma_{xx,\text{fvm}})}{t_x} \times 100\% \tag{41}$$

Table 2. Mesh convergence study for stress concentration around a circular hole

Mesh size	RMS$_{\sigma_{xx}}$ (Pa)
1,450	16.32
5,800	5.28
23,200	1.79
98,000	0.62
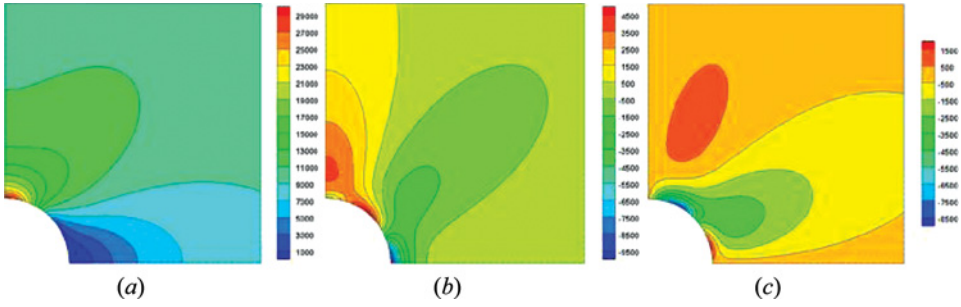
Figure 11. Contours of stress (Pa) for FVM scheme: (a) σ_{xx}; (b) σ_{yy}; (c) σ_{xy} (color figure available online).

The contours show that the errors are maximum in the area of stress concentration. However, mesh skewness also leads to some errors.

8.4. Transient Vibration of Fixed-Free Beams

The temporal accuracy of the FVM solver is tested by studying the undamped vibration of a fixed-free cantilever beam subjected to shear stress at the free end. A schematic of the beam is shown in Figure 13. The natural frequency Ω of a fixed-free cantilever beam [57] can be derived as

$$\Omega = \frac{3.516}{2\pi L^2} \sqrt{\frac{EI}{\rho bh}} \tag{42}$$

where b is the width, h is the thickness, and ρ is the density of the beam. Young's modulus, Poisson's ratio, and the density of the beam are taken to be $E = 200$ GPa, $\nu = 0.31$, and $\rho = 7{,}854$ kg/m^3, respectively. For the above fixed-free beam, the natural frequency is calculated according to Eq. (42) to be $\Omega = 8.15$ Hz. To simulate this problem, the beam is assumed to have $\mathbf{w} = 0$ and $\partial \mathbf{w}/\partial t = 0$ as the initial conditions. At time $t = 0$, a shear stress $\tau = 1{,}000$ Pa is applied on the right face. The top and bottom faces are assumed to be traction-free surfaces, and the left face is constrained to
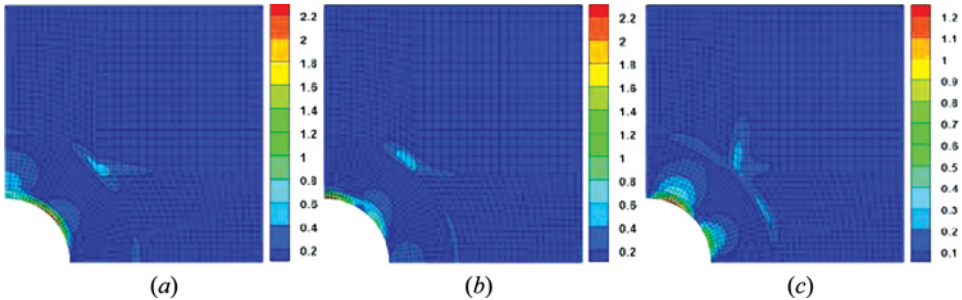

Figure 12. Contours of percentage absolute errors in stresses: (a) δ_{xx}; (b) δ_{yy}; (c) δ_{xy} (color figure available online).
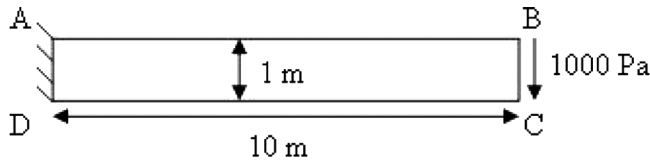
Figure 13. Cantilever beam subjected to shear stress at the free end.

have zero displacement. The applied shear stress on the right face is linearly ramped up for the first 0.02 s, and then maintained at $\tau = 1,000$ Pa. This causes the beam to vibrate in a sinusoidal motion with the above-mentioned natural frequency. A plane stress condition is assumed and a 9×100 mesh is used for this problem. The time step in this problem is taken to be $\Delta t = 10^{-5}$ s, which gives a maximum wave speed Courant number of Co $= 0.5$, where the Courant number Co is defined as

$$Co = u \frac{\Delta t}{\Delta x} \tag{43}$$

Here u is the unconfined solid wave speed given by

$$u = \sqrt{\frac{E}{\rho}} \tag{44}$$

The deflection at the neutral axis on the free end of the beam is shown in Figure 14 as a function of time. The FVM result for natural frequency of the beam is $\Omega = 8.106$ Hz. Thus the FVM result for natural frequency is within 0.55% of the analytical result.
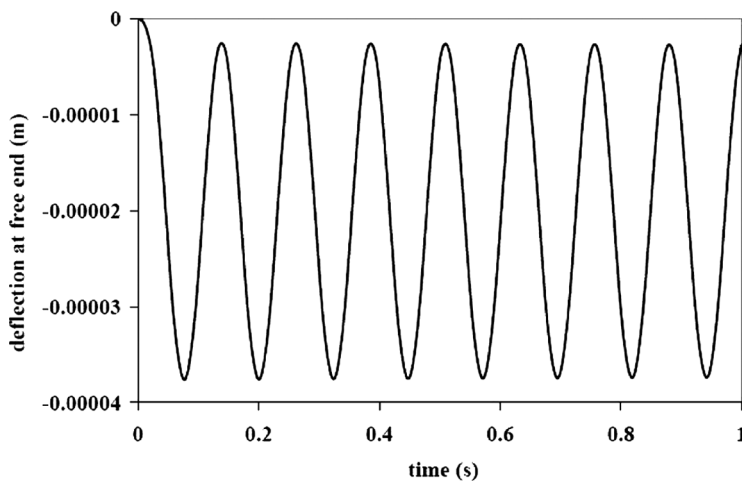

Figure 14. Temporal variation of the deflection at the free end of the cantilever beam.

8.5. Structural Deformation Due to Electrostatic Actuation in MEMS

The FV solver is next applied to study structure–electrostatic interaction in MEMS. The goal is to study structural deformation of a MEMS device, treated as a fixed-fixed beam under electrostatic actuation. A schematic of the MEMS device is shown in Figure 3. The electrostatic force is treated as a surface force on the top electrode, and is assumed to be a nonlinear function of the gap width. Young's modulus of the material is $E = 200$ GPa, and Poisson's ratio is $\nu = 0.31$. The beam has length of 400 μm and thickness of 4 μm. A $20 \times 1,000$ mesh is selected for this simulation based on a mesh convergence study, and a plane stress condition is assumed. For this problem the governing equation for electrostatic potential, Eq. (20), is not solved in the air gap. Instead, to obtain the electrostatic force on the top electrode, the potential gradient is approximated as

$$\left[\frac{\partial\phi}{\partial y}\right]_{\text{air}} = \frac{\phi_{\text{top}} - \phi_{\text{bottom}}}{\Delta h} \tag{45}$$

where Δh is the width of the air gap, and ϕ_{top} and ϕ_{bottom} represent the electrostatic potential on the top electrode and bottom electrode, respectively.

The boundary conditions are as follows: The left and right sides are specified as zero-displacement surfaces, the top surface is a traction-free surface, while the electrostatic force calculated from Eq. (22) is applied on the bottom surface. If the deflection of the top electrode is small, then the electrostatic force can be assumed to be a constant. In that case, the problem becomes that of a fixed-fixed beam subjected to uniform loading of the magnitude of the electrostatic force per unit length. Then the deflection of the beam is given by Eq. (38). The deflection expression in Eq. (38) can be nondimensionalized in the following way to give a potential difference independent expression for the deflection:

$$w_y^* = w_y\left(\frac{24EI}{\alpha}\right) \tag{46}$$

For cases where the electrostatic force is variable and is a nonlinear function of the gap width, the deflection of the top electrode is nondimensionalized in the same manner as in Eq. (46), with α calculated for the corresponding constant electrostatic force case with the same potential difference applied between the two electrodes. The nondimensional deflection of the beam is calculated for potential differences of 10 V, 50 V, 100 V, and 160 V, and the results are shown in Figure 15, which also shows the nondimensional deflection for the constant electrostatic force case. As is evident, for a 10 V potential difference between the top and bottom electrodes, the deflection calculated by the FVM solver is almost the same as the deflection for the constant-force case. The nondimensional deflection calculated for the variable-force case increases with an increase in the potential difference between the two electrodes, and for 160 V applied potential difference between the two electrodes, the maximum nondimensional deflection is greater by around 36% than the corresponding constant-force case. The maximum deflection at the bottom surface of the top electrode is shown in Table 3 for the variable electrostatic force case. It is observed that
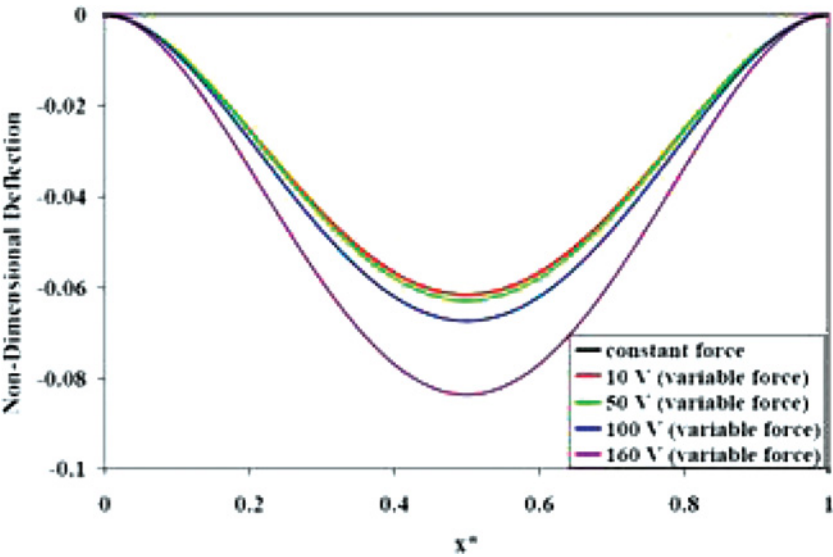
Figure 15. Nondimensional deflection of the top electrode (color figure available online).

for 160 V applied potential difference between the two electrodes, the maximum deflection of the top electrode is -6.74×10^{-7} m.

8.6. Pull-In Voltage in MEMS

The methodology developed in this article is used next to study quasi-static and dynamic pull-in voltages for an RF MEMS switch shown in Figure 3. Young's modulus of the material is $E = 200$ GPa, and Poisson's ratio is $\nu = 0.31$. The top electrode has length of 400 μm and thickness of 4 μm. When a dc voltage is applied across the two surfaces, an electrostatic force F_{elec}, given by Eq. (22), is induced which pulls down the top electrode. The electrostatic force is a nonlinear function of the gap width, and varies as $F_{elec} \sim g^{-2}$, where g is the gap width. The restoring mechanical force F_m varies linearly as the change in gap width, $F_m \sim g_0 - g$, where g_0 is the zero-voltage gap width. An equilibrium position is reached when these two forces balance each other. However, as the dc voltage is increased beyond a critical limit called the pull-in voltage V_{PI}, the restoring mechanical force can no longer

Table 3. Maximum deflection of the top electrode for the variable-force case

Potential difference (V)	Maximum deflection (m)
10	-1.94×10^{-9}
50	-4.94×10^{-8}
100	-2.12×10^{-7}
160	-6.74×10^{-7}

balance the electrostatic force, and the gap closes. A simplified expression of pull-in voltage is obtained as [58]

$$V_{PI} = \sqrt{\frac{8K_{eff}g_0^3}{27\varepsilon_0 A_{eff}}} \tag{47}$$

where ε_0 is the permittivity of free space. For a fixed-fixed beam, K_{eff} is given as

$$K_{eff} = \frac{32\widehat{E}bh^3}{L^3} \tag{48}$$

where $\widehat{E}$ is the modified Young's modulus. $\widehat{E}$ is equal to E if $b \sim h$, and is equal to $E/(1-\nu^2)$ if $b > 5h$. The effects of residual stress, nonlinear stiffening, and axial stretching have been neglected in deriving Eq. (47). Furthermore, if the effects of charge redistribution and fringing fields are neglected, then the effective electrode area A_{eff} can simply be expressed as bL.

Two cases are simulated to study the pull-in phenomenon. In the first case, the bottom electrode has the same length as the top electrode, as shown in Figure 3. In the second case, the bottom electrode has a length of 80 μm, as shown in Figure 16. A $20 \times 1,000$ mesh is selected for both the structural solver and the electrostatics solver. To obtain quasi-static deflection of the beam, the electrostatic field is first solved in the air gap using Eq. (20). The electrostatic force on the top electrode is then calculated using Eq. (22). One outer iteration for the structural deformation of the top electrode is then performed. The cell-based displacements are subsequently interpolated to obtain nodal displacements, which are used to deform the structural mesh. The mesh for the air gap is then adjusted using the nodal displacements on the top electrode–air interface as a Dirichlet boundary condition and employing distance-weighted smoothing of the mesh. The electrostatic field in the air gap is again solved using Eq. (20), and the entire process is repeated until convergence. For the dynamic analysis, the entire procedure is repeated over a number of time steps. The time step in the dynamic analysis is taken to be $\Delta t = 8.8 \times 10^{-9}$ s, which is about 1/1,000th of the pull-in time.

The maximum deflection at the bottom surface of the top electrode is shown in Figure 17 as a function of the applied voltage. It is observed that for the case in which the bottom electrode has the same length as the top electrode, the pull-in voltage is around 181 V. The analytical solution for pull-in voltage is also shown in the
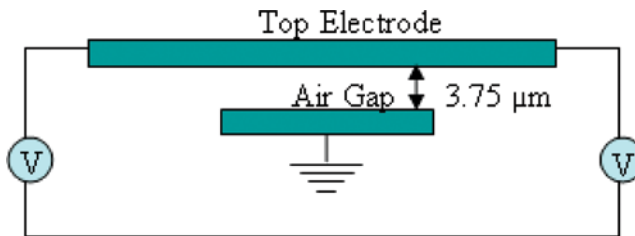

Figure 16. RF MEMS with partial bottom electrode (color figure available online).
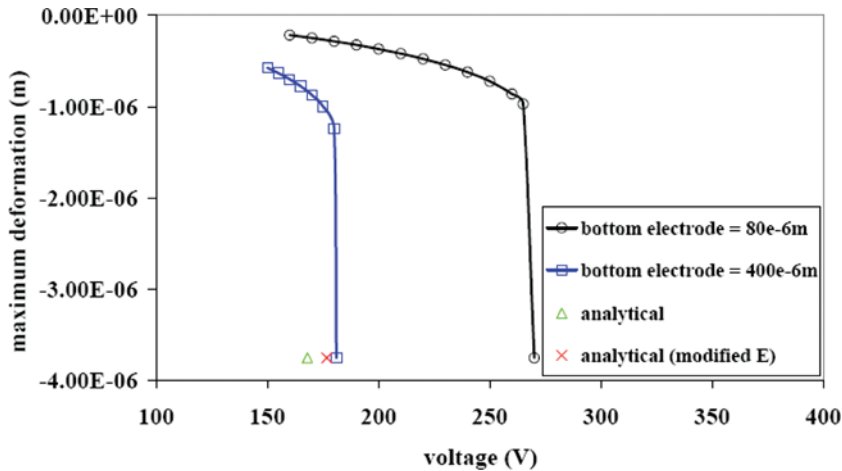
Figure 17. Quasi-static pull-in voltage for RF MEMS (color figure available online).

plot. It is observed that the analytical pull-in voltages with actual and modified Young's modulus are around 168 V and 177 V, respectively. It should be noted that the analytical solution assumes that the bottom electrode has the same length as the top electrode. It is further seen that the pull-in voltage for the case of partial bottom electrode is around 270 V. With partial bottom electrode, the electrostatic force is applied only over the middle region of the beam. Thus it requires a larger force to deform the structure, which results in a higher pull-in voltage. The dynamic pull-in voltage for the case when both of the electrodes have the same length is found to be 165 V. Thus the dynamic pull-in voltage is less than the corresponding quasi-static pull-in voltage by around 9%. This result is similar to what has been reported in [59].

9. CONCLUSIONS AND FUTURE WORK

In this article, a cell-based FV solver for structural analysis has been developed. The FVM scheme involves second-order spatial discretization and first-order temporal discretization of the governing equation for structural dynamics. The discretized algebraic equations are solved using a BCGSTAB solver. The convergence rate of the FV methodology is improved dramatically by implementing complete linearization of the stress tensor, which enables the fully implicit FVM discretization of the governing equation. This enables the computation of linear structural deformation problems within one iteration of the outer loop, and decreases the computational time by approximately a factor of 200. The FVM solver has been verified on three different test cases: (1) deformation of a fixed-free beam with concentrated load at the free end, (2) stress concentration around a circular hole, and (3) transient vibration of fixed-free beams. The FVM solver for structural dynamics is then applied to study the deformation of a movable electrode, treated as a fixed-fixed beam, under electrostatic actuation. Results indicate that the maximum nondimensional beam deflection increases by around 36% at a potential difference of 160 V if the electrostatic force is assumed to be a nonlinear function of the gap width,

instead of being a constant. The quasi-static and dynamic pull-in voltages for the RF MEMS device are then evaluated. It is found that the simulation value of the pull-in voltage (181 V) matches relatively well with the approximate theoretical value (177 V). It is also observed that the dynamic pull-in village is less than the quasi-static pull-in voltage by around 9%.

The article demonstrates that robust and accurate solvers based on the finite-volume method may be developed for structure–electrostatics interaction. Efforts are underway to couple the structural solver to a finite-volume-based fluid flow solver to study dynamic structural deformation under electrostatic loads. Results from this effort will be reported in due course.

REFERENCES

1. G. M. Rebeiz, *RF MEMS: Theory, Design and Technology*, Wiley, New Jersey, 2003.
2. D. Peroulis, *Personal communication*, Purdue University, 2010.
3. O. C. Zienkiewicz, *The Finite Element Method*, McGraw-Hill, New York, 1977.
4. J. H. Ferziger and M. Perić, *Computational Methods for Fluid Dynamics*, Springer-Verlag, Berlin, 1999.
5. E. Oñate, M. Cervera, and O. C. Zienkiewicz, A Finite Volume Format for Structural Mechanics, *Int. J. Numer. Meth. Eng.*, vol. 37, pp. 181–201, 1994.
6. S. R. Idelsohn and E. Oñate, Finite Volumes and Finite Elements: Two 'Good Friends', *Int. J. Numer. Meth. Eng.*, vol. 37, pp. 3323–3341, 1994.
7. J. N. Reddy and D. K. Gartling, *The Finite Element Method in Heat Transfer and Fluid Dynamics*, CRC Press, Ann Arbor, MI, 1994.
8. J. Donea and A. Huerta, *Finite Element Methods for Flow Problems*, Wiley, Chichester, UK, 2003.
9. O. C. Zienkiewicz, R. L. Taylor, and P. Nithiarasu, *The Finite Element Method for Fluid Dynamics*, 6th ed., Elsevier, Amsterdam, 2005.
10. J. Donea, S. Giuliani, and J. P. Halleux, An Arbitrary Lagrangian-Eulerian Finite Element Method for Transient Dynamic Fluid-Structure Interactions, *Comput. Meth. Appl. Mech. Eng.*, vol. 33, pp. 689–723, 1982.
11. T. Nomura, ALE Finite Element Computations of Fluid-Structure Interaction Problems, *Comput. Meth. Appl. Mech. Eng.*, vol. 112, pp. 291–308, 1994.
12. W. Dettmer and D. Perić, A Computational Framework for Fluid-Structure Interaction: Finite Element Formulation and Applications, *Comput. Meth. Appl. Mech. Eng.*, vol. 195, pp. 5754–5779, 2006.
13. T. E. Tezduyar, Stabilized Finite Element Formulations for Incompressible Flow Computations, *Adv. Appl. Mech.*, vol. 28, pp. 1–44, 1992.
14. T. E. Tezduyar, M. Behr, and J. Liou, A New Strategy for Finite Element Computations Involving Moving Boundaries and Interfaces—The Deforming-Spatial-Domain/Space-Time Procedure: I. The Concept and the Preliminary Numerical Tests, *Comput. Meth. Appl. Mech. Eng.*, vol. 94, pp. 339–351, 1992.
15. T. E. Tezduyar, M. Behr, S. Mittal, and J. Liou, A New Strategy for Finite Element Computations Involving Moving Boundaries and Interfaces—The Deforming-Spatial-Domain/Space-Time Procedure: II. Computation of Free-Surface Flows, Two-Liquid Flows, and Flows with Drifting Cylinders, *Comput. Meth. Appl. Mech. Eng.*, vol. 94, pp. 353–371, 1992.
16. T. E. Tezduyar, Finite Element Methods for Flow Problems with Moving Boundaries and Interfaces, *Arch. Comput. Meth. Eng.*, vol. 8, pp. 83–130, 2001.

17. K. J. Bathe and H. Zhang, A Flow-Condition-Based Interpolation Finite Element Procedure for Incompressible Fluid Flows, *Comput. Struct.*, vol. 80, pp. 1267–1277, 2002.
18. H. Kohno and K. J. Bathe, A Flow-Condition-Based Interpolation Finite Element Procedure for Triangular Grids, *Int. J. Numer. Meth. Fluids*, vol. 49, pp. 849–875, 2005.
19. H. Kohno and K. J. Bathe, Insight into the Flow-Condition-Based Interpolation Finite Element Approach: Solution of Steady-State Advection Diffusion Problems, *Int. J. Numer. Meth. Eng.*, vol. 63, pp. 197–217, 2005.
20. H. Kohno and K. J. Bathe, A Nine-Node Quadrilateral FCBI Element for Incompressible Fluid Flows, *Commun. Numer. Meth. Eng.*, vol. 22, pp. 917–931, 2006.
21. K. J. Bathe and H. Zhang, Finite Element Developments for General Fluid Flows with Structural Interactions, *Int. J. Numer. Meth. Eng.*, vol. 60, pp. 213–232, 2004.
22. T. Grätsch and K. J. Bathe, Goal-Oriented Error Estimation in the Analysis of Fluid Flows with Structural Interactions, *Comput. Meth. Appl. Mech. Eng.*, vol. 195, pp. 5673–5684, 2006.
23. I. Demirdžić, P. Martinović, and A. Ivanković, Numerical Simulation of Thermal Deformation in Welded Workpiece, *Zavarivanje*, vol. 31, pp. 209–219, 1988.
24. I. Demirdžić and S. Muzaferija, Finite Volume Method for Stress Analysis in Complex Domains, *Int. J. Numer. Meth. Eng.*, vol. 37, pp. 3751–3766, 1994.
25. I. Demirdžić, and S. Muzaferija, Numerical Method for Coupled Fluid Flow, Heat Transfer and Stress Analysis Using Unstructured Moving Meshes with Cells of Arbitrary Topology, *Comput. Meth. Appl. Mech. Eng.*, vol. 125, pp. 235–255, 1995.
26. H. Jasak and H. G. Weller, Application of the Finite Volume Method and Unstructured Meshes to Linear Elasticity, *Int. J. Numer. Meth. Eng.*, vol. 48, pp. 267–287, 2000.
27. I. Demirdžić and D. Martinović, Finite Volume Method for Thermo-Elasto-Plastic Stress Analysis, *Comput. Meth. Appl. Mech. Eng.*, vol. 109, pp. 331–349, 1993.
28. J. Fainberg and H. J. Leister, Finite Volume Multigrid Solver for Thermo-Elastic Stress Analysis in Anisotropic Materials, *Comput. Meth. Appl. Mech. Eng.*, vol. 137, pp. 167–174, 1996.
29. Y. D. Fryer, C. Bailey, M. Cross, and C. H. Lai, A Control Volume Procedure for Solving the Elastic Stress-Strain Equations on an Unstructured Mesh, *Appl. Math. Model.*, vol. 15, pp. 639–645, 1991.
30. C. Bailey and M. Cross, A Finite Volume Procedure to Solve Elastic Solid Mechanics Problems in Three Dimensions on an Unstructured Mesh, *Int. J. Numer. Meth. Eng.*, vol. 38, pp. 1757–1776, 1995.
31. G. A. Taylor, C. Bailey, and M. Cross, Solution of the Elastic/Visco-Plastic Constitutive Equations: A Finite Volume Approach, *Appl. Math. Model.*, vol. 19, pp. 746–760, 1995.
32. A. K. Slone, C. Bailey, and M. Cross, Dynamic Solid Mechanics Using Finite Volume Methods, *Appl. Math. Model.*, vol. 27, pp. 69–87, 2003.
33. A. K. Slone, K. Pericleous, C. Bailey, and M. Cross, Dynamic Fluid-Structure Interaction using Finite Volume Unstructured Mesh Procedures, *Comput. Struct.*, vol. 80, pp. 371–390, 2002.
34. S. V. Patankar and D. B. Spalding, A Calculation Procedure for Heat, Mass and Momentum Transfer in Three-Dimensional Parabolic Flows, *Int. J. Heat Mass Transfer*, vol. 15, pp. 1787–1806, 1972.
35. J. P. van Doormaal and G. D. Raithby, Enhancements of the SIMPLE Method for Predicting Incompressible Fluid Flows, *Numer. Heat Transfer*, vol. 7, pp. 147–163, 1984.
36. Y. Jiang and A. J. Przekwas, Implicit, Pressure-Based Incompressible Navier-Stokes Equations Solver for Unstructured Meshes, AIAA-94-0305, 1994.
37. B. R. Baliga, A Control-Volume Based Finite Element Method for Convective Heat and Mass Transfer, Ph.D. thesis, University of Minnesota, Minneapolis, MN, 1978.

38. C. Prakash and S. V. Patankar, A Control Volume-Based Finite-Element Method for Solving the Navier-Stokes Equations Using Equal-Order Velocity-Pressure Interpolation, *Numer. Heat Transfer*, vol. 8, pp. 259–280, 1985.

39. Y.-Y. Tsui and T.-C. Wu, Use of Characteristic-Based Flux Limiters in a Pressure-Based Unstructured-Grid Algorithm Incorporating High-Resolution Schemes, *Numer. Heat Transfer B*, vol. 55, pp. 14–34, 2009.

40. C. Prakash, Examination of the Upwind (Donor-Cell) Formulation in Control Volume Finite-Element Methods for Fluid Flow and Heat Transfer, *Numer. Heat Transfer*, vol. 11, pp. 401–416, 1987.

41. J. P. Wang, A. G. L. Borthwick, and R. Eatock Taylor, Finite-Volume-Type VOF Method on Dynamically Adaptive Quadtree Grids, *Int. J. Numer. Meth. Fluids*, vol. 45, pp. 485–508, 2004.

42. V. Costa, L. Oliveira, B. Baliga, and A. Sousa, Simulation of Coupled Flows in Adjacent Porous and Open Domains Using a Control-Volume Finite-Element Method, *Numer. Heat Transfer A*, vol. 45, pp. 675–697, 2004.

43. A. Teskeredžić, I. Demirdžić, and S. Muzaferija, Numerical Method for Heat Transfer, Fluid Flow, and Stress Analysis in Phase-Change Problems, *Numer. Heat Transfer B*, vol. 42, pp. 437–459, 2002.

44. C.-H. Cheng and C.-Y. Wu, An Approach Combining Body-Fitted Grid Generation and Conjugate Gradient Methods for Shape Design in Heat Conduction Problems, *Numer. Heat Transfer B*, vol. 37, pp. 69–83, 2000.

45. C. Kim, M. Y. Kim, M. J. Yu, and S. C. Mishra, Unstructured Polygonal Finite-Volume Solutions of Radiative Heat Transfer in a Complex Axisymmetric Enclosure, *Numer. Heat Transfer B*, vol. 57, pp. 227–239, 2010.

46. M. B. Salah, F. Askri, and S. B. Nasrallah, Unstructured Control-Volume Finite-Element Method for Radiative Heat Transfer in a Complex 2-D Geometry, *Numer. Heat Transfer B*, vol. 48, pp. 477–497, 2005.

47. J. Y. Murthy and S. R. Mathur, Computation of Sub-micron Thermal Transport Using an Unstructured Finite Volume Method, *J. Heat Transfer*, vol. 124, pp. 1176–1181, 2002.

48. D. Pope and G. Gogos, A New Multicomponent Diffusion Formulation for the Finite-Volume Method: Application to Convective Droplet Combustion, *Numer. Heat Transfer B*, vol. 48, pp. 213–233, 2005.

49. S. R. Mathur and J. Y. Murthy, A Pressure-Based Method for Unstructured Meshes, *Numer. Heat Transfer B*, vol. 31, pp. 195–215, 1997.

50. T. J. Barth, Aspects of Unstructured Grids and Finite-Volume Solvers for the Euler and Navier-Stokes Equations, Special Course on Unstructured Grid Methods for Advection-Dominated Flows, AGARD Report 787, 1992.

51. Y. Xu and N. R. Aluru, Pull-In/Out Analysis of Nano/Microelectromechanical Switches with Defective Oxide Layers, *Appl. Phys. Lett.*, vol. 95, pp. 073112, 2009.

52. Y. Zhao and A. Forhad, A General Method for Simulation of Fluid Flows with Moving and Compliant Boundaries on Unstructured Grids, *Comput. Meth. Appl. Mech. Eng.*, vol. 192, pp. 4439–4466, 2003.

53. J. L. Bentley, Multidimensional Binary Search Trees Used for Associative Searching, *Commun. ACM*, vol. 18, pp. 509–517, 1975.

54. R. Barrett, M. Berry, T. F. Chan, J. Demmel, J. Donato, J. Dongarra, V. Eijkhout, R. Pozo, C. Romine, and H. V. D. Vorst, *Templates for the Solution of Linear Systems: Building Blocks for Iterative Methods*, SIAM, Philadelphia, PA, 1994.

55. I. Demirdžić, S. Muzaferija, and M. Perić, Benchmark Solutions of Some Structural Analysis Problems using Finite Volume Method and Multigrid Acceleration, *Int. J. Numer. Meth. Eng.*, vol. 40, pp. 1893–1908, 1997.

56. S. P. Timoshenko and J. N. Goodier, *Theory of Elasticity*, McGraw-Hill, New York, 1970.

57. M. Petyt, *Introduction to Finite Element Vibration Analysis*, Cambridge University Press, Cambridge, UK, 1998.

58. H. C. Nathanson, W. E. Newell, R. A. Wickstrom, and J. R. Davis, Jr., The Resonant Gate Transistor, *IEEE Trans. Electron. Devices*, vol. 14, pp. 117–133, 1967.

59. G. K. Ananthasuresh, R. K. Gupta, and S. D. Senturia, An Approach to Macromodeling of MEMS for Nonlinear Dynamic Simulation, *Microelectromechanical Systems (MEMS), ASME Dynamic Systems and Control (DSC) Series*, vol. 59, pp. 401–407, 1996.